Lattice Heat Backflow Dynamics in Bi-metallic Nanolayers Subjected to Ultrafast Laser Heating

Milad Mozafarifard^a, Yan Wang^a

^aDepartment of Mechanical Engineering, University of Nevada, Reno, Reno, 89557, NV, USA

Abstract

Understanding and controlling thermal transport in heterostructures is critical for optimizing thermal management strategies for optoelectronic devices and laser manufacturing processes. In this study, employing two-temperature Boltzmann transport equation simulations, we systematically investigate the lattice heat backflow behavior in bi-metallic nanolayers. This phenomenon arises when a sublayer with strong electron-phonon coupling attains a higher phonon temperature than the top layer directly exposed to laser irradiation. Specifically, we analyze the impact of layer thickness, electron-phonon coupling strength of the top layer and interlayer, interfacial thermal conductance, and laser pulse duration on the lattice heat backflow behavior. Our theoretical insights offer guidance for optimizing this behavior in tailored thermal management applications.

1. Introduction

Electron-phonon coupled thermal transport plays a pivotal role in dictating the thermal characteristics of micro-/nano-scale electronic and optoelectronic devices [1, 2, 3, 4, 5]. These devices often feature metal-nonmetal interfaces among their micro-/nano-sized components. The phenomenon is equally relevant in laser manufacturing [6, 7] and electron or phonon spectroscopy [8, 9], where nonequilibrium states of electrons and phonons arise due to laser-induced heating or the presence of metal-nonmetal interfaces in manufacturing feedstocks, measured samples, or their connections to substrates or transducers for absorbing laser heat. Understanding and quantifying the impact of electron-phonon coupling and nonequilibrium states on overall thermal transport, especially the evolution of the temperature field in both space and time coordinates, is crucial in these scenarios.

Considerable research efforts have been dedicated to understanding thermal transport across solid-solid interfaces, particularly involving metals and nonmetals [10]. It is now well-established that phonons predominantly govern thermal transport across nonmetal-nonmetal interfaces [10, 11]. In low-temperature regimes, phonon transmission occurs predominantly through elastic mechanisms, dictating the overall thermal conductance. However, at higher temperatures, the inelastic transmission of phonons becomes increasingly significant [12, 13, 14]. In unique scenarios involving superlattice structures with periodically or aperiodically arranged interfaces, coherent phonon transport, scattering phenomena, and localization behavior may manifest [15, 16, 17].

Various atomistic strategies have been proposed to enhance interfacial thermal transport across nonmetal-nonmetal interfaces, with the primary objective of reducing phonon interfacial thermal resistance (R_{pp}) . These strategies include interface alloying, interface nanostructuring, and phonon bridging, among others [18, 19, 20, 21]. Additionally, macroscopic approaches such as the application of thermal interface materials have been explored.

In contrast, electrons typically serve as the dominant heat carriers across metal-metal interfaces. Cahill et al. introduced a diffuse-mismatch model for electrons, which demonstrates reasonable agreement with experimental data [22]. Notably, the electron interfacial thermal resistance (R_{ee}) between metals can be 1-2 orders of magnitude lower than the phonon interfacial thermal resistance R_{pp} . Consequently, metal-metal interfaces generally exhibit significantly lower thermal resistance compared to metal-nonmetal or nonmetal-metal interfaces.

Thermal transport across a metal-nonmetal interface presents another intriguing scenario, wherein, in most cases, phonons can carry heat across the interface while electrons can hardly transmit into the nonmetal side. Consequently, there is a nonequilibrium between electrons and phonons near the interface, a phenomenon that has garnered significant attention in recent years [3, 4]. An illustrative example is the enhancement of heat dissipation in devices incorporating a metal film-on-nonmetal substrate configuration, such as those found in heat-assisted magnetic recording or integrated circuits [23, 24, 25]. Effective dissipation becomes imperative to cool the heat-generating metallic components subjected to heating by intense electromagnetic waves (e.g., lasers) or Joule heating [26]. However, theoretical, computational, and experimental studies have consistently identified an interfacial thermal resistance

stemming from electron-phonon nonequilibrium at metal-nonmetal interfaces [3, 4, 27]. Notably, this resistance, expressed as $R_{ep} = [\kappa_e/(\kappa_e + \kappa_p)]^{1.5}/\sqrt{g_{ep}\kappa_p}$, where κ_e , κ_p , and g_{ep} denote the electronic thermal conductivity, phonon thermal conductivity, and electron-phonon coupling factor of the metal component. R_{ep} can be substantial for metals with low g_{ep} , like gold or copper, hindering heat dissipation across the metal film-nonmetal substrate interface.

To address the imperative of reducing R_{ep} between metal-nonmetal interfaces for enhanced heat dissipation, it was proposed to add a thin layer of metal with a high g_{ep} , such as titanium or chromium [23]. This strategic addition effectively reduces the R_{ep} term. The mechanism involves the high electronic thermal conductance between the original metal thin film and the metallic interlayer. As a result, hotter electrons in the thin film rapidly transmit into the metallic interlayer, and, owing to the large g_{ep} of the interlayer, the hot electrons promptly deposit heat into phonons in the interlayer lattice, thus rapidly reducing electron-phonon nonequilibrium. This strategy, proposed in Ref. [23], was later validated through Boltzmann transport simulations (BTE) [25] and experiments [28, 29, 30, 31]. Notably, in 2019, Li et al. demonstrated reduced thermal resistance of Au-Al₂O₃ interface with an interlayer of Ni, which has nearly two orders of magnitude stronger electron-phonon coupling than Au [29]. In 2022, Oommen et al. demonstrated increased thermal conductance between Au and Al_2O_3 with an interlayer of Al, Ni, and Cr, all with stronger electron-phonon coupling than Au [30]. Moreover, in 2023, Lin et al., with combined two-temperature modeling and transient thermal reflectance experiments, demonstrated notably enhanced heat transfer across Au- Al_2O_3 interface and Au-Si interface by inserting an interlayer of Ni [31].

Beyond its effectiveness in reducing g_{ep} , an intriguing phenomenon was observed through BTE simulations: under ultrafast laser heating, the lattice temperature of the interlayer could surpass that of the top thin film. In this scenario, the laser effectively heats up the interlayer beneath the top layer and induces a backflow of lattice heat from the interlayer to the top layer—a seemingly counterintuitive behavior elucidated by two-temperature model-based BTE simulations [25].

While the backflow phenomenon was observed in the laser pump-probe experiments of Au-Cr-Au tri-metallic layer structures in 1994 [6], it garnered little attention until more recent strategies aimed at reducing R_{ep} between metals and nonmetals. In 2014, Choi et

al. demonstrated the practical application of this backflow phenomenon by using it to heat up a platinum layer beneath a gold layer, achieving a unique approach for pump-probe measurements of the electron-phonon coupling factor of gold [32].

Despite these studies, the comprehensive understanding of how the thermal transport properties of the metallic top layer-metallic interlayer-nonmetallic substrate system, including electronic and phonon characteristics and interfacial resistances, influence overall thermal transport characteristics—especially the backflow behaviors—remains unknown. This knowledge gap hinders the wider and further application of this unique thermal transport behavior.

In this work, we systematically investigate the lattice heat backflow dynamics in a configuration featured by a bi-metallic layer supported on a nonmetal substrate, employing Au-Pt-Si and Au-Al-Si as model systems. Our approach involves rigorous two-temperature BTE simulations to unravel the intricate interplay of electronic and phonon thermal transport properties, electron-phonon coupling factors, and interfacial resistances, shedding light on the underlying mechanisms governing the observed backflow phenomena.

2. Methodology

In this study, we employ the two-temperature Boltzmann transport equation (2T-BTE) approach to characterize electron-phonon coupled interfacial thermal transport in metal-metal-nonmetal nanolayers exposed to ultrashort laser irradiation. The BTE is utilized to model both the electron and phonon subsystems of the top metallic layer, allowing for their coupling via the electron-phonon coupling factor (g_{ep}) , as outlined below:

$$\frac{\partial e_e}{\partial t} + \boldsymbol{v_e} \cdot \boldsymbol{\nabla} e_e = -\frac{e_e - e_e^0}{\tau_e} - g_{ep}(T_e - T_p) + S, \tag{1a}$$

$$\frac{\partial e_p}{\partial t} + \boldsymbol{v_p} \cdot \boldsymbol{\nabla} e_p = -\frac{e_p - e_p^0}{\tau_p} + g_{ep}(T_e - T_p), \tag{1b}$$

where e, e^0 , v, and τ represent the energy density, the equilibrium energy density, velocity, and relaxation time of heat carriers, respectively. The g_{ep} is electron-phonon coupling factor, T is the temperature, and the subscripts e and p represent the electron and phonon subsystems, respectively. S is the volumetric heat source term, which mimics an ultrafast laser

pulse in the following form [33],

$$S(x,t) = \frac{0.94(1-R)J}{t_{pulse}\left(\delta + \delta_b\right) \left[1 - exp\left(-\frac{L}{\delta + \delta_b}\right)\right]} exp\left[\frac{-x}{\delta + \delta_p} - 2.77\left(\frac{t}{t_{pulse}}\right)^2\right],\tag{2}$$

where R is the reflectance of the top layer surface, J is the laser fluence, t_{pulse} is the laser pulse duration, δ is the optical penetration depth, δ_b is the electron ballistic length, and L is the top layer thickness.

The energy can be related to temperature based on e = CT, in which C is the heat capacity. For a phonon subsystem above its Debye temperature, $e_p = C_p T_p$, where C_p is a constant. In contrast, the electronic heat capacity is temperature-dependent, which, based on the Sommerfeld expansion, is expressed as $C_e = \gamma_e T_e$. This results in $e_e = \gamma_e T_e^2$, where γ_e is the electron heat capacity constant [34].

The 2T-BTE for the metallic top layer is solved using the D1Q2 lattice Boltzmann (LBM) method for one-dimensional thermal transport (D1), in which there are two discrete velocity directions (Q2), often represented as + and - for forward and backward directions, respectively. The discretized form of 2T-BTE is thus [35, 36],

$$e_{e,\alpha}(x + \Delta x_e, t + \Delta t) = [1 - \omega_e] e_{e,\alpha}(x, t) + \omega_e e_{e,\alpha}^0(x, t)$$

$$- g_{ep} \left[\frac{e_{e,\alpha}^0(x, t)}{C_e} - \frac{e_{p,\alpha}^0(x, t)}{C_p} \right] \Delta t + S \Delta t,$$
(3a)

$$e_{p,\alpha}(x + \Delta x_p, t + \Delta t) = [1 - \omega_p] e_{p,\alpha}(x, t) + \omega_p e_p^0(x, t)$$

$$+ g_{ep} \left[\frac{e_{e,\alpha}^0(x, t)}{C_e} - \frac{e_{p,\alpha}^0(x, t)}{C_p} \right] \Delta t.$$
(3b)

In Eqs. (3a) and (3b), the subscript α denotes forward (+) and backward (-) directions, and $\omega_e = \Delta t/\tau_e$ and $\omega_p = \Delta t/\tau_p$ are the scattering weight factors for electron and phonon respectively, wherein Δt is the time step. In addition, e_e^0 and e_p^0 can be approximated as $(e_{e,+} + e_{e,-})/2$ and $(e_{p,+} + e_{p,-})/2$. It must be mentioned that the nodal spacing (computational grid size) is linked to the time step by $\Delta x_e = v_e \Delta t$ and $\Delta x_p = v_p \Delta t$ for electron and phonon, respectively. This results in significant differences between the nodal spacing of electrons and phonons, as illustrated in Fig. 1. Notably, they can differ by nearly three orders of magnitude in certain cases, because v_e is on the order of $\sim 10^6$ m/s while v_p is on the order of $\sim 10^3$ m/s. Thus, one electron nodal spacing is often coupled to thousands of phonon nodal spacing in our simulations.

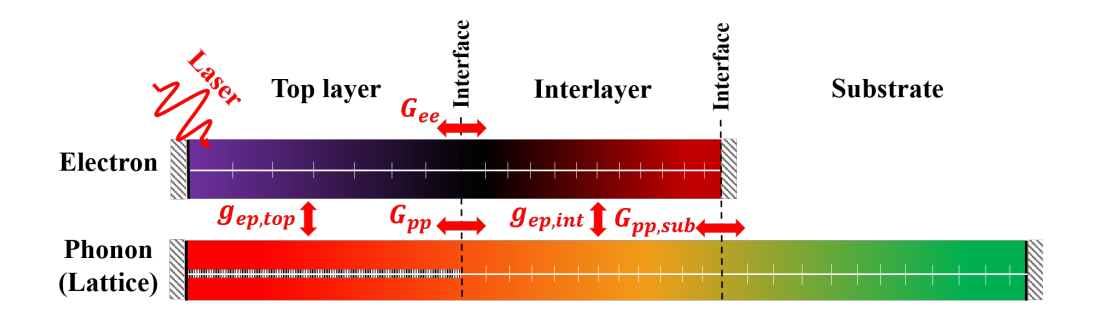


Figure 1: The schematic illustration depicts the grid arrangement and boundary conditions at the interface of different layers. The left and right boundaries of the electron and phonon grids are implemented with the adiabatic boundary condition. Additionally, the laser heating of electrons at the top layer is modeled as a source term described by Eq. 2. In the electron channel, the connection between the top layer and interlayer for electron thermal transport across the interface is facilitated by the G_{ee} term. Meanwhile, in the phonon channel, the top layer and interlayer are linked through the G_{pp} term for interfacial phonon thermal transport. Additionally, the interlayer and substrate are coupled via $G_{pp,sub}$. The color maps superimposed on the electron and phonon grids represent a typical scenario of electron and phonon temperature distributions obtained from our 2T-BTE simulations.

To simulate electron-phonon coupled thermal transport in the metallic interlayer and in the Si substrate, the diffusive two-temperature model (TTM) is applied,

$$C_e \frac{\partial T_e}{\partial t} = \nabla \cdot (\kappa_e \nabla T_e) - g_{ep}(T_e - T_p) + S, \tag{4a}$$

$$C_p \frac{\partial T_p}{\partial t} = \nabla \cdot (\kappa_p \nabla T_p) + g_{ep}(T_e - T_p), \tag{4b}$$

where κ and C represent thermal conductivity and heat capacity respectively. The explicit finite difference scheme with a uniform computational grid size is employed to discretize the TTM. The first-order time-derivative and second-order space-derivative terms in Eq. (4) are approximated based on the forward and central differencing in time and space respectively, resulting in discretized forms as

$$T_{e}(x, t + \Delta t) = (1 - 2\Lambda_{e} - \Gamma_{e}) T_{e}(x, t) + \Lambda_{e} [T_{e}(x + \Delta x, t) + T_{e}(x - \Delta x, t)] + \Gamma_{e}T_{p}(x, t) + \Gamma_{e}S/g_{ep},$$

$$T_{p}(x, t + \Delta t) = (1 - 2\Lambda_{p} - \Gamma_{p}) T_{p}(x, t) + \Lambda_{p} [T_{p}(x + \Delta x, t) + T_{p}(x - \Delta x, t)] + \Gamma_{p}T_{e}(x, t),$$
(5b)

where $\Lambda_e = \kappa_e \Delta t/c_e \Delta x^2$, $\Gamma_e = g_{ep} \Delta t/C_e$, $\Lambda_p = \kappa_p \Delta t/c_p \Delta x^2$, and $\Gamma_p = g_{ep} \Delta t/C_p$.

Equations (3a), (3b), (5a), and (5b) are solved simultaneously to simulate electronphonon coupled interfacial thermal transport, capturing diverse thermal behaviors in this
work. These range from ballistic transport in the nanolayers to diffusive behavior in the Si
substrate. The values of all the phonon or electron properties of Au, Pt, Al, and Si used
in our 2T-BTE simulations are taken from Ref. [25]. Notably, the electron and phonon
velocities were evaluated from experimental data or first-principles calculations assuming a
gray model of electrons and phonons. It is crucial to acknowledge that these values serve as
effective representations of electron and phonon velocities tailored specifically for gray Boltzmann transport models. A more sophisticated treatment of electron and phonon transport
would necessitate the consideration of distinct velocities for various electron bands or phonon
branches. However, in the context of our present work aimed at elucidating the influence of
diverse electron and phonon characteristics on lattice heat backflow behavior, the adoption
of the gray model alongside its associated properties suffices to achieve our objectives.

It is important to highlight that key electron and phonon properties, such as g_{ep} , C_e , and κ_p , can exhibit significant temperature dependence. In our study, we constrain the maximum electron temperature to approximately 3,000 K or below—a range where g_{ep} remains relatively constant, while C_e scales linearly with electron temperature, as per the Sommerfeld model. Hence, we assert that neglecting the temperature dependence of g_{ep} and employing the Sommerfeld model for C_e is a reasonable approximation for our purposes. However, for scenarios where electron temperatures exceed 3,000 K significantly, we recommend considering the temperature-dependent properties of g_{ep} and C_e .

Furthermore, it is noteworthy that the lattice thermal conductivity κ_p of metals such as Au, Pt, and Al also varies with lattice temperature. However, as demonstrated in the Supplementary Materials, we demonstrate that these variations do not exert a significant impact on phonon temperature, thereby not altering the conclusions drawn regarding lattice heat backflow behavior.

In our model, we consider two forms of interfacial thermal transport: electronic thermal transport across metal-metal interfaces (the conductance G_{ee}), and phonon thermal transport across both metal-metal and metal-nonmetal interfaces (the conductance G_{pp}). It has been reported that a unique form of interfacial thermal transport, stemming from the direct

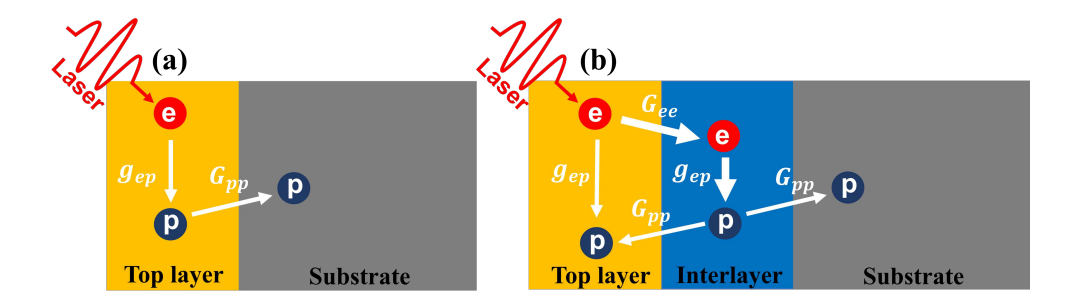


Figure 2: Schematic of nanolayer structures, (a) without an interlayer, and (b) with an interlayer.

coupling between metal electrons and nonmetal phonons, can also significantly contribute to heat transfer across metal-nonmetal interfaces. This phenomenon typically occurs when the electron temperature exceeds 3,000 K or even 4,000 K, especially when the d-band electrons in the metal are excited by ultrafast laser irradiation [37, 33]. However, since the maximum electron temperature considered in our study mostly remains below this threshold, we neglect this interfacial thermal transport mechanism.

3. Results and Discussion

As illustrated in Fig. 2a, in a single-metallic-layer structure supported on a nonmetallic substrate (Fig. 2a), heat dissipation occurs through a single pathway: from the top layer to the substrate beneath. Here, the laser energy absorbed by electrons in the metallic layer is initially transferred to the lattice (phonons), which then propagates to the lattice of the substrate. Conversely, in bi-metallic layers supported on a nonmetal substrate (Fig. 2b), two potential pathways exist. Firstly, akin to the scenario in Fig. 2a, hot electrons in the top layer may initially transfer heat to its phonons, which subsequently propagate to the phonons in the interlayer. The second pathway, crucial for the phenomenon of lattice heat backflow, involves hot electrons in the top layer first transitioning into the interlayer, where they deposit heat into the interlayer's phonons. If this second pathway predominates over the first, resulting in the interlayer's phonon or lattice temperature exceeding that of the top layer, heat can then flow from the interlayer lattice back to the top layer lattice. This intricate lattice heat backflow behavior constitutes the focal point of investigation in this study.

In this section, we systematically analyze the lattice heat backflow dynamics in Au/Pt/Si

systems, characterized by bi-metallic layers of Au and Pt. Additionally, in Supplementary Materials, we provide our 2T-BTE simulation results for Au/Al/Si systems, which exhibit similar backflow behaviors albeit with distinct values attributable to the differing material properties of the Pt and Al interlayers. The parameters investigated in this study include the thickness and electron-phonon coupling factor of both the top layer and the interlayer, the thermal conductance between these layers, and the duration of the laser pulse.

3.1. Effect of top layer thickness

Noting the top layer thickness (L_{top}) as a crucial factor in determining the overall thermal transport behavior of the bi-metallic-layer structure, we conduct 2T-BTE simulations on a series of structures with a Au top layer thickness ranging from 10 nm to 200 nm, all exhibiting lattice heat backflow behavior but at varying levels. As illustrated in Figs. 3a-c, L_{top} significantly influences the electron temperature response at the front and rear surfaces of the top layer. Specifically, in the case of a 10 nm-thick top layer (Fig. 3a), electrons at the front surface can reach a temperature of 3,000 K. Conversely, for the 200 nm-thick structure (Fig. 3c), the peak electron temperature at the front surface of the top layer is only approximately 1,100 K. These results are reasonable because laser energy absorbed in regions close to the front surface can rapidly transfer to the rear end of the Au top layer, thereby reducing the front surface temperature. Thus, a thicker top layer can accommodate more heat from the top surface region, thus more significantly reducing the temperature there.

Furthermore, it is evident that as the top layer becomes thicker, a greater temperature difference emerges between the front and rear surfaces of the top layer. This observation aligns with our expectation that a thicker film, with its larger overall heat capacitance, can absorb more heat itself rather than heating up its rear end and the interlayer underneath. Specifically, as indicated by the blue curve in Fig. 3c, the electron temperature at the front surface of the interlayer reaches ~ 450 K, much lower than the maximum interlayer electron temperature of $\sim 1,100$ K and ~ 780 K attained in the 10 nm-thick and 50 nm-thick cases, respectively.

Consequently, due to the lower interlayer electron temperature in the thicker-top-layer structures, phonons in the interlayer correspondingly reach a lower peak temperature, as evident when comparing Figs. 3d-f. Quantitatively, the interlayer phonon temperature (at

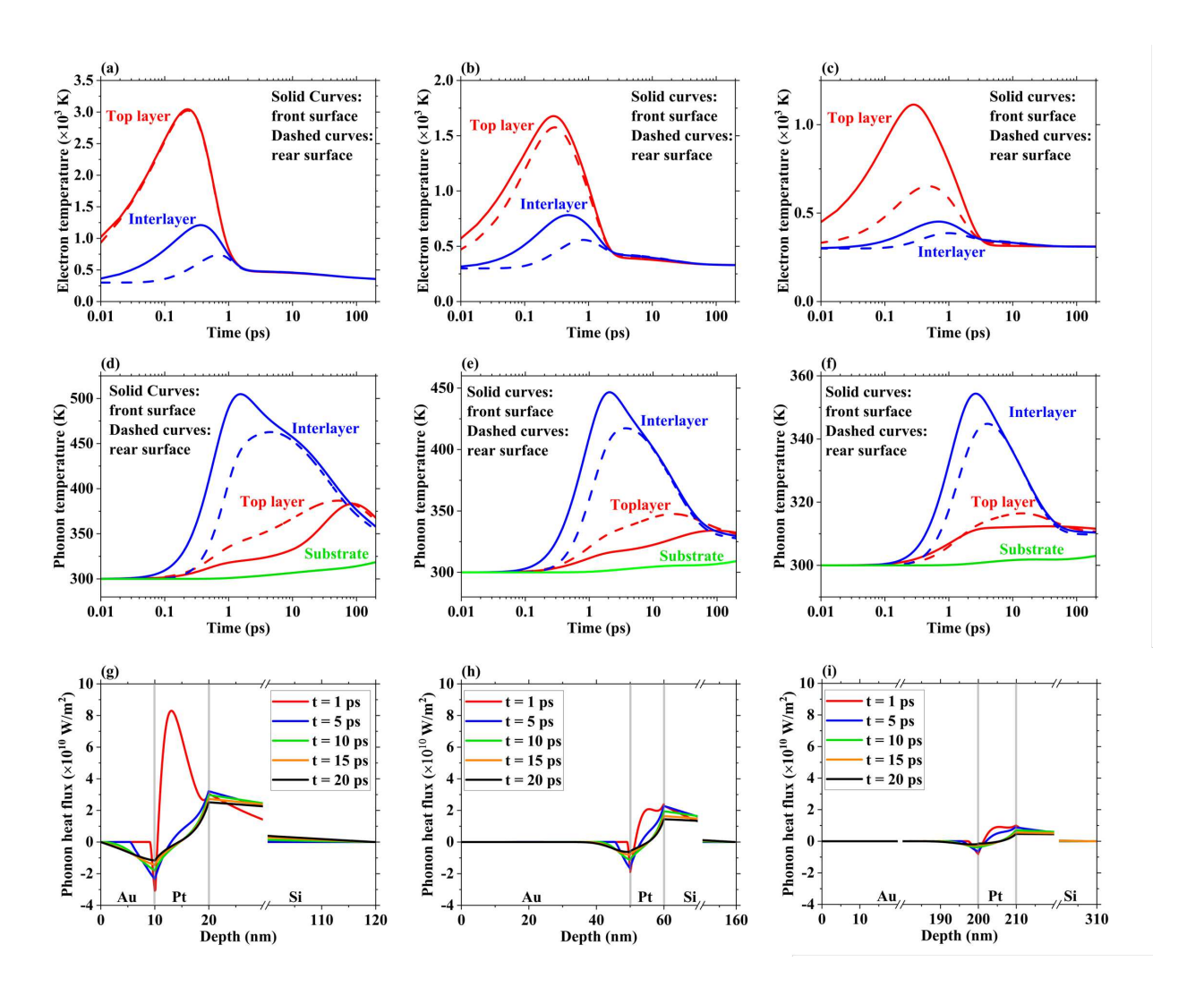


Figure 3: Electron temperature, phonon temperature, and phonon heat flux of Au/Pt/Si nanolayer with different Au top layer thicknesses. First column (panels a, d, and g): 10nm-Au/10nm-Pt/100nm-Si. Second column (panels b, e, and h): 50nm-Au/10nm-Pt/100nm-Si. Third column (panels c, f, and i): 200nm-Au/10nm-Pt/100nm-Si.

the front surface) reaches a maximum value of ~ 500 K in the 10-nm-top-layer structure, while it is only 354 K in the 200-nm-top-layer case. Despite this, in all three cases, the interlayer phonons are warmer than those in the top layer, exhibiting a robust lattice heat backflow behavior. Further confirmation is provided by the heat flux profile (i.e., as a function of depth into the films), where regions close to the top layer-interlayer interface display notably negative heat flux, indicating the backflow of heat from interlayer to the top layer phonon.

Hence, we can deduce that a thinner top layer (i.e., smaller L_{top}) leads to a more pronounced lattice heat backflow, underscoring the importance of this parameter in design considerations. Remarkably, it is noteworthy that this phenomenon persists even when the top layer thickness L_{top} scales up to 200 nm, albeit with a decrease in magnitude.

3.2. Effect of interlayer thickness

Figure 4 presents the data for Au/Pt/Si structures with varying Pt interlayer thicknesses (L_{int}) of 10 nm, 50 nm, and 200 nm. In Fig. 4a, the phonon temperature profile displays a noticeable peak within the interlayer, diminishing significantly from the top layer-interlayer interface (at 10 nm depth) to the front surface of the top layer. Fig. 4b, featuring an increased L_{int} of 50 nm, reveals a distinct temperature gradient inside the interlayer, indicative of substantial heat transfer into the substrate rather than back to the top film. This gradient becomes more pronounced in Fig. 4c for $L_{int} = 200$ nm. In both the 50 nm (Fig. 4b) and 200 nm (Fig. 4c) cases, the phonon temperature peak is very close to the interface (10 nm depth) between the top layer and interlayer, suggesting pronounced heat flow in further deep into the interlayer (i.e., positive depth direction) rather than back to the top layer.

Figures 4d-f depict the evolution of phonon temperature at the front and rear surfaces of the top layer and interlayer. Comparing Fig. 4d, Fig. 4e, and Fig. 4f, several key observations emerge regarding the influence of interlayer thickness on heat transfer within the Au/Pt/Si structures. Firstly, the phonon temperature at the front surface of the interlayer is minimally affected by interlayer thickness, as phonons near the top layer-interlayer interface are primarily heated by the hot electrons transmitted from the Au top layer. In fact, as shown in Figs. 4a-c, the peak phonon temperature in the interlayer is nearly the same for the three structures, which is mainly affected by L_{top} , thus leading to similar phonon temperature at the front surface of the interlayer. However, the phonon temperature at the rear surface of

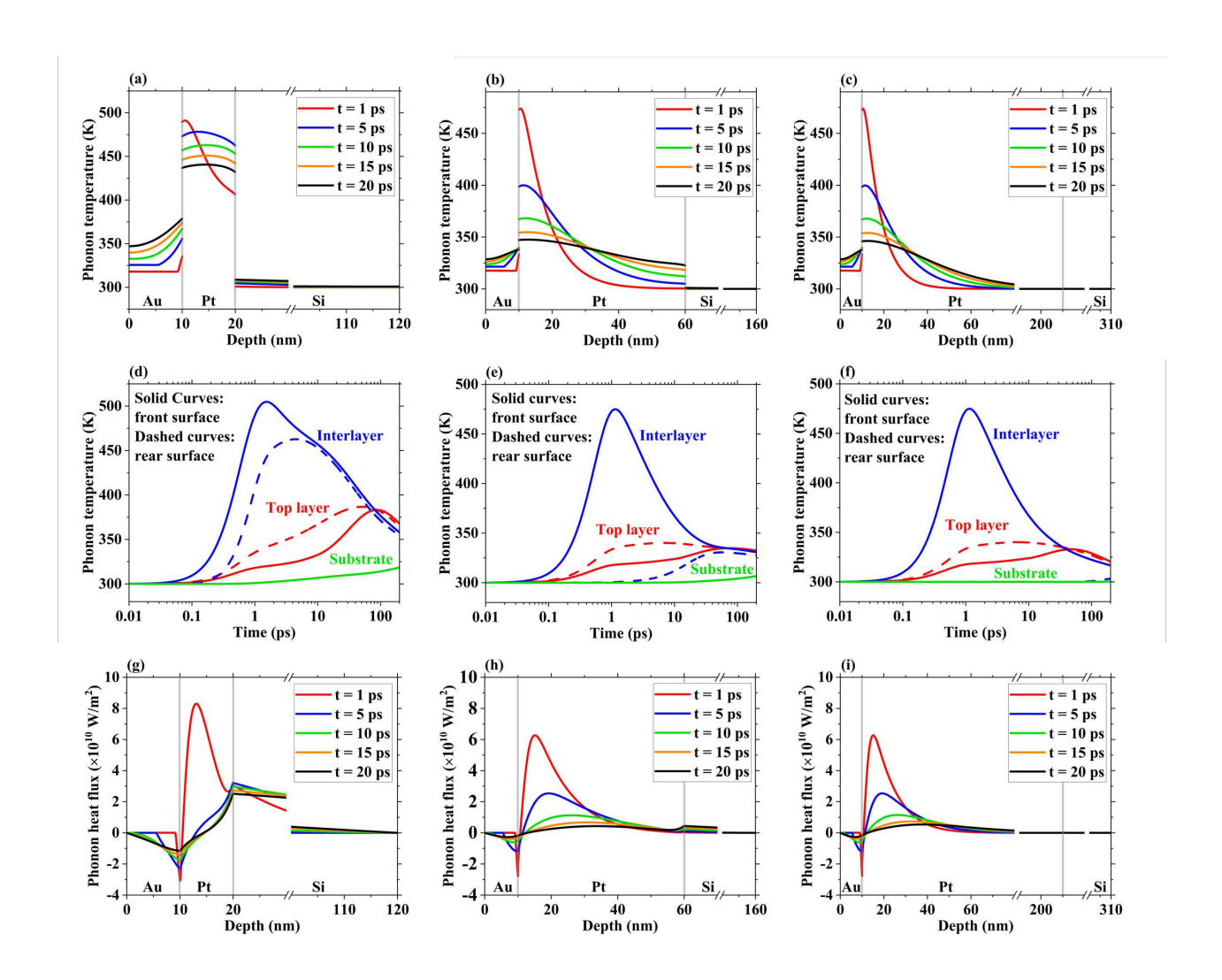


Figure 4: Electron temperature, phonon temperature, and phonon heat flux of Au/Pt/Si nanolayer with different Pt interlayer thicknesses. First column (panels a, d, and g): 10nm-Au/10nm-Pt/100nm-Si. Second column (panels b, e, and h): 10nm-Au/50nm-Pt/100nm-Si. Third column (panels c, f, and i): 10nm-Au/200nm-Pt/100nm-Si.

the interlayer significantly decreases with an increase in interlayer thickness. This is rationalized by the larger bulk phonon thermal resistance of the interlayer, scaling with L_{int} as $R_{t,int} = L_{int}/\kappa_{int}$. This effect is evident in Figs. 4b and c, where the phonon temperature exhibits a substantial gradient inside the interlayer.

As depicted in Figs. 4g-i, the duration of phonon heat backflow markedly diminishes in structures with thicker interlayers. Specifically, the backflow heat flux maintains an order of magnitude of $-1 \times 10^{10} W/m^2$ in the 10-nm interlayer case (Fig. 4g) even at 20 ps after the laser pulse irradiation, whereas it reduces to only $-0.2 \times 10^{10} W/m^2$ in the 200-nm interlayer case at 20 ps. Consequently, we can infer that L_{int} must be sufficiently small to exhibit a significant lattice heat backflow.

3.3. Effect of g_{ep} of top layer

In this investigation, the top layer consists of Au, a metal widely acknowledged for possessing one of the lowest values of g_{ep} among common elemental metals [34]. As depicted in Fig. 2, the anticipation is that the value of g_{ep} can wield a substantial influence on heat backflow, as it governs the distribution of the laser energy absorbed by top layer electrons into two distinct channels: either to the top layer phonons or to the interlayer electrons (and subsequently its phonons). Therefore, a comprehensive exploration of the effect of g_{ep} on the overall thermal transport characteristics of the bi-metallic layer structure is essential, necessitating the variation of its value relative to the original value in Au for a quantitative, parametric study.

As depicted in Figs. 5a, d, and g, g_{ep} significantly influences the evolution of electron temperature in the top layer. Specifically, a higher g_{ep} accelerates the cooling process of laser-heated electrons in the top layer. Correspondingly, as illustrated in Figs. 5b, e, and h, the phonon temperature in the top layer rises at a faster rate and reaches a higher value in top layers with an elevated g_{ep} due to a more rapid and substantial heat transfer from hot electrons. Specifically, the peak phonon temperature at the rear surface of the top layer is 379 K, 413 K, and 468 K in Fig. 5b $(g_{ep,Au})$, e $(10g_{ep,Au})$, and h $(40g_{ep,Au})$, respectively.

In instances with higher g_{ep} of the top layer, a reduced fraction of heat is directed towards the interlayer. As illustrated in Figs. 5b, e, and h, the peak phonon temperature at the front surface of the interlayer declines from 510 K in Fig. 5b $(g_{ep,Au})$ to 434 K in Fig. 5e $(10g_{ep,Au})$,

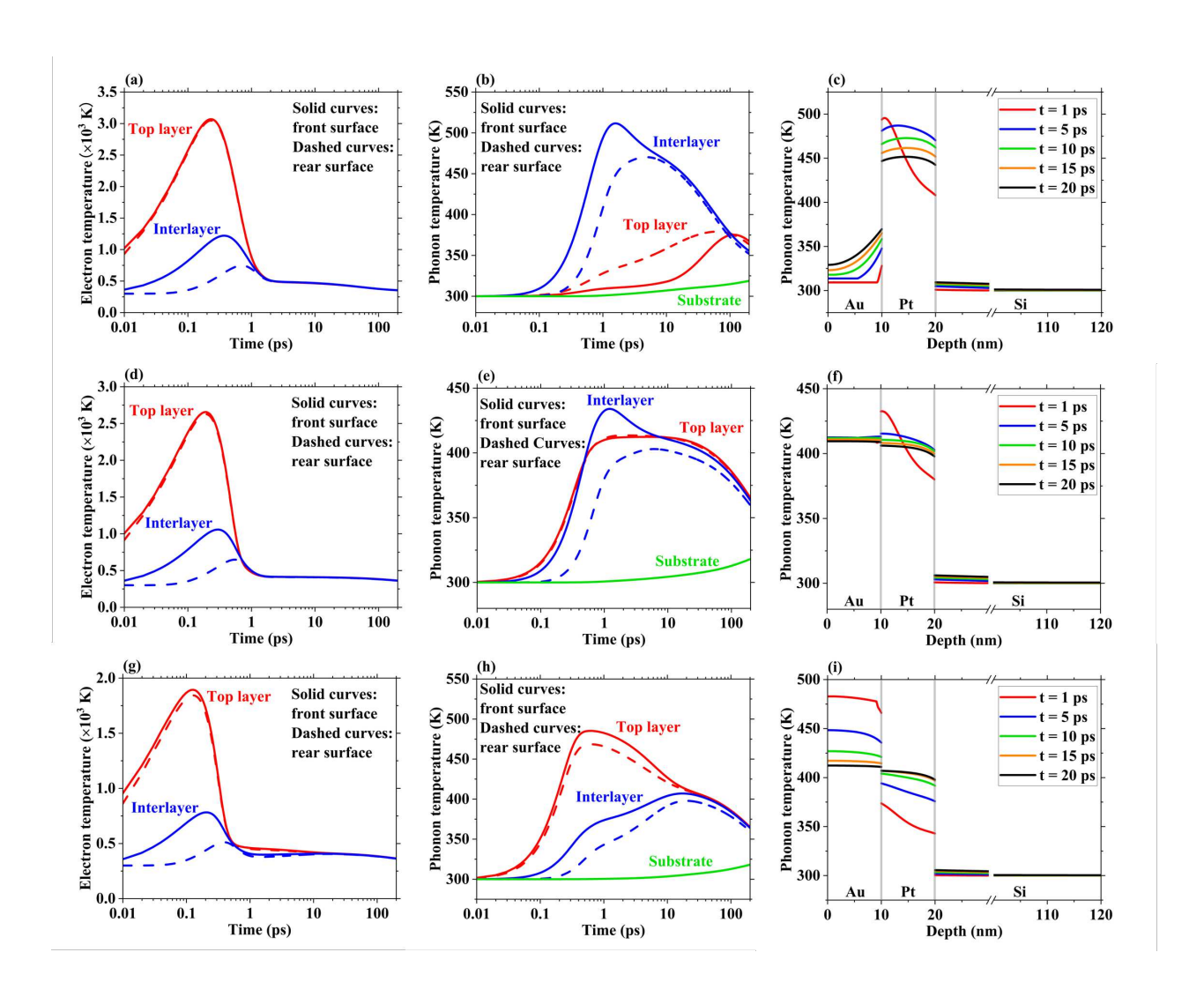


Figure 5: Electron and phonon temperatures of 10nm-Au/10nm-Pt/100nm-Si nanolayer with varying values of g_{ep} of Au top layer (multiples of the original value of Au $g_{ep,Au}$). First row (panels a, b, and c): $0.5g_{ep,Au}$. Second row (panels d, e, and f): $10g_{ep,Au}$. Third row (panels g, h, and i): $40g_{ep,Au}$.

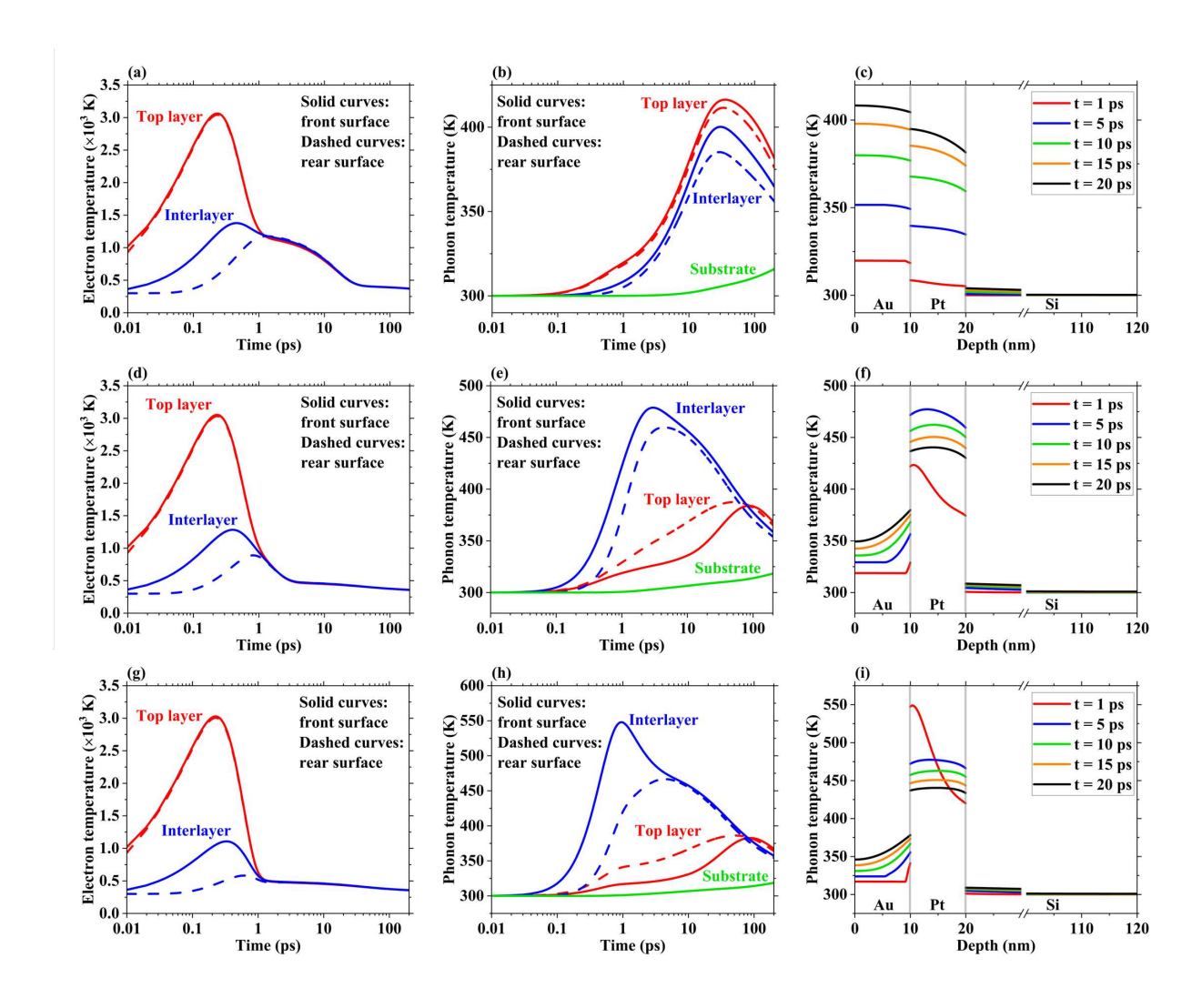


Figure 6: Electron and phonon temperatures of 10nm-Au/10nm-Pt/100nm-Si nanolayer with different values of g_{ep} of Pt interlayer (multiples of the original g_{ep} value of Pt, i.e., $g_{ep,Pt}$). First row (panels a, b, and c): $0.025g_{ep,Pt}$. Second row (panels d, e, and f): $0.5g_{ep,Pt}$. Third row (panels g, h, and i): $2g_{ep,Pt}$.

and eventually to 407 K in Fig. 5h ($40g_{ep,Au}$). Notably, in Fig. 5h, the interlayer phonon temperature falls below that of the top layer, resulting in only forward flow of heat from the top layer to the interlayer. This can also be observed in phonon temperature profile, Fig. 5i, where the phonon temperature of top layer at the interface is greater than that of interlayer, meaning that heat is flowing from top layer to interlayer phonon.

3.4. Effect of g_{ep} of interlayer

For comparative analysis, we also investigate the impact of g_{ep} of the interlayer on the thermal transport characteristics of the bi-metallic-layer system. As depicted in Fig. 6a-c, it

significantly influences the evolution of electron temperature in the top layer, albeit not to the same extent as the effect of g_{ep} of the top layer, as presented in Figs. 5a-c. Its influence on the electron and phonon temperatures in the interlayer is direct and prominent, as it directly dictates heat transfer between them. As illustrated in Fig. 6d-f, in interlayers with a higher g_{ep} , electron temperature experiences a faster decline, while phonon temperature exhibits a more rapid increase, indicating a greater potential for the backflow of heat to the top layer lattice. Furthermore, since electrons can deposit heat more rapidly in the interlayer region, a larger portion of the heat in the laser-heated hot electrons in the top layer preferentially transfers to the interlayer, rather than to the top layer lattice, resulting in a lower phonon temperature of the top layer. These two factors synergistically amplify the temperature difference between the interlayer and the top layer, thereby promoting the backflow of heat from the interlayer to the top layer. This is substantiated by the phonon temperature profiles in Figs. 6c, f, and i, where the case with the highest g_{ep} of the interlayer exhibits more significant phonon temperature difference at the top layer-interlayer interface, in which the higher phonon temperature of interlayer indicates the backflow of heat from interlayer to top layer phonon (Fig. 6i). However, for lower values of interlayer g_{ep} , Fig. 6c, the phonon temperature of top layer at the top layer-interlayer interface is always greater than that of interlayer, meaning that for this case, the heat always flows in positive direction from top layer to the interlayer phonon.

Through the discussions above on the impact of g_{ep} on both the top layer and interlayer, we can draw immediate conclusions regarding their influence on the lattice heat backflow phenomenon. Firstly, a higher g_{ep} of the top layer impedes backflow, as it diverts more heat to the phonons of the top layer itself rather than heating the interlayer. Secondly, an elevated g_{ep} of the interlayer promotes the backflow phenomenon by simultaneously increasing the phonon temperature of the interlayer and reducing that of the top layer. Thirdly, as demonstrated by the cases in Fig. 5i and Fig. 6c, the lattice heat backflow behavior disappears when the g_{ep} of the top layer exceeds that of the interlayer.

3.5. Effect of interfacial thermal conductance

The quality of the interface, influenced by factors such as interface air gaps, species mixing, or defects like dislocations, directly impacts the interfacial thermal resistance (R)

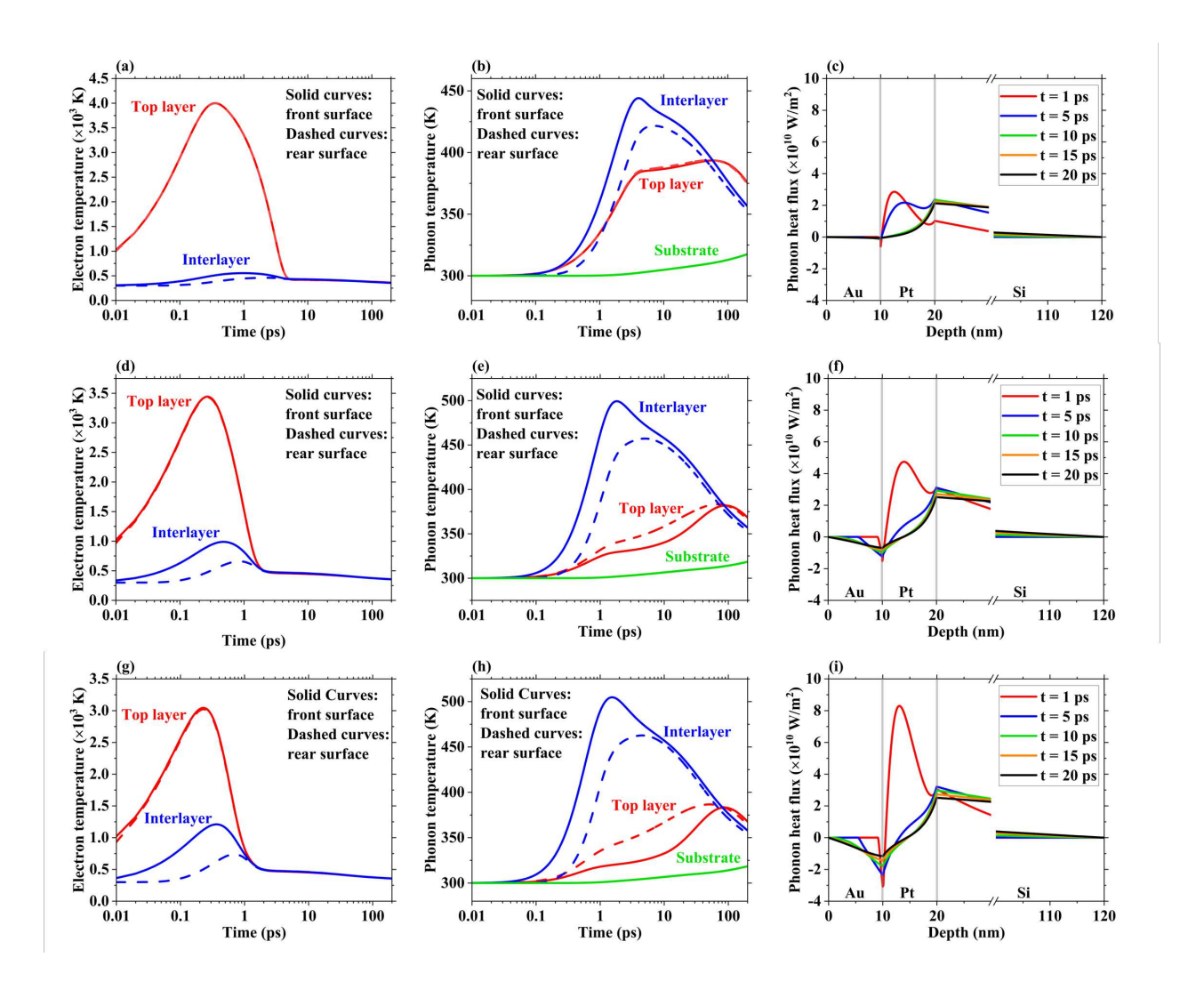


Figure 7: Electron temperature, phonon temperature, and phonon heat flux of 10nm-Au/10nm-Pt/100nm-Si nanolayer with different factors of interfacial thermal conductance. First row (panels a, b, and c): $0.1G_{ee}$ (G_{pp}). Second row (panels d, e, and f): $0.5G_{ee}$ (G_{pp}). Third row (panels g, h, and i): $1G_{ee}$ (G_{pp}).

and thus interfacial thermal conductance (G) between the top layer and interlayer. In this study, we examine the effects of both electronic interfacial thermal conductance $(G_{ee} = R_{ee}^{-1})$ and phononic interfacial thermal conductance $(G_{pp} = R_{pp}^{-1})$ on the thermal transport characteristics of the bi-metallic-layer structure. To simplify the problem, we assume that changes in G_{ee} and G_{pp} occur in the same ratio when we vary their values. Figure 7 presents our 2T-BTE results, demonstrating the impact of scaling the original values of G_{ee} and G_{pp} by factors of 0.1 and 0.5.

Illustrated in Figs. 7a, d, and g, G_{ee} significantly influences the electron cooling dynamics

in the top layer. This outcome aligns with expectations since G_{ee} dictates the speed of electronic heat transfer into the interlayer; consequently, a higher G_{ee} accelerates the cooling process of the laser-heated hot electrons in the top layer. Correspondingly, we observe a more rapid rise in both electron (Figs. 7a, d, and g) and phonon temperatures (Figs. 7b, e, and h) in the interlayer with an increase in scaling of interfacial thermal conductance from $0.1G_{ee}$ to G_{ee} . These effects, working synergistically, amplify the temperature difference between the front surface of the interlayer and the rear surface of the top layer, thereby promoting lattice heat backflow.

The impact of increasing G_{pp} on lattice heat backflow, although a secondary factor in comparison to G_{ee} and g_{ep} , is still significant. Given its direct influence on thermal transport from interlayer phonons to the top layer, a higher value of G_{pp} is expected to expedite lattice heat backflow. However, it is important to note that unlike G_{ee} or g_{ep} (for both top layer and interlayer), G_{pp} does not affect the "potential" of lattice heat backflow. In other words, it does not determine whether the interlayer lattice can attain a higher temperature than the top layer lattice. Consequently, in scenarios where the top layer consistently maintains a higher temperature than the interlayer—such as when the g_{ep} of the former is higher than that of the latter or when G_{ee} is too small—a higher G_{pp} solely promotes the forward flow of heat from the top layer to the interlayer, rather than backflow. Nevertheless, it remains crucial to maintain a sufficiently large G_{pp} to ensure efficient backflow when the condition $T_{p,interlayer} > T_{p,toplayer}$ is met. The results in Figs. 7c, f, and i confirm this assertion, displaying more significant phonon backflow (negative) heat flux in the region of Au/Pt interface.

3.6. Effect of laser pulse duration

Finally, we investigate the influence of laser pulse duration (t_{pulse}) on the phonon heat backflow behavior, acknowledging its crucial role as a variable in laser manufacturing and spectroscopy processes.

In our simulations, we maintain the total fluence of the laser pulse constant and solely vary t_{pulse} . As illustrated in Figs.8a, d, and g, for $t_{pulse} = 0.04$ ps, 4 ps, and 10 ps, respectively, the application of a femtosecond laser (Fig. 8a) elevates the electron temperature in the top layer to a maximum of 4,150 K, while the $t_{pulse} = 10$ ps case (Fig. 8g) only raises the

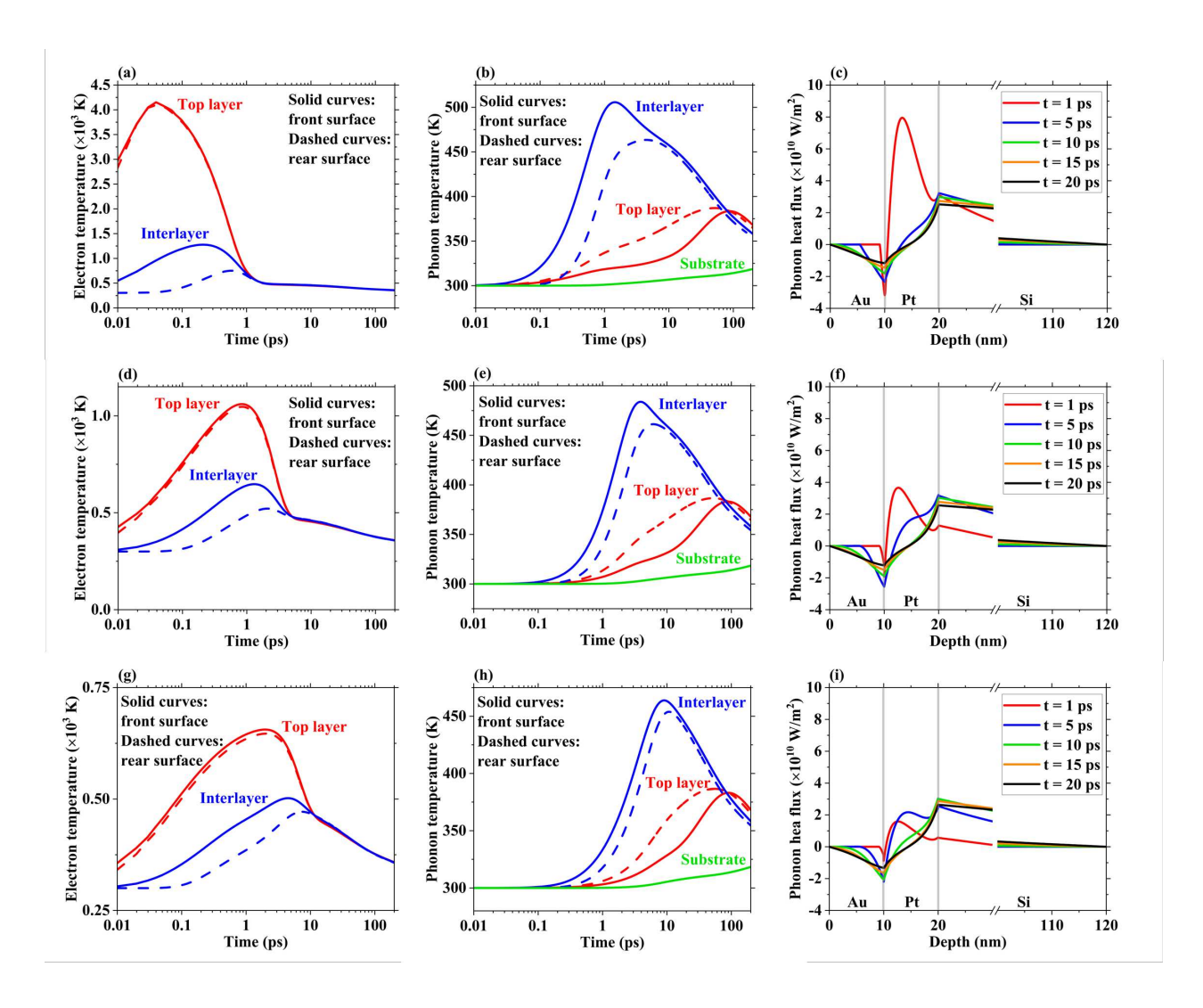


Figure 8: Electron temperature, phonon temperature, and phonon heat flux of 10nm-Au/10nm-Pt/100nm-Si nanolayer with different values of laser pulse duration. First row (panels a, b, and c): $t_{pulse} = 0.04$ ps. Second row (panels d, e, and f): $t_{pulse} = 4$ ps. Third row (panels g, h, and i): $t_{pulse} = 10$ ps.

electron temperature to 650 K. Similarly, the peak electron temperature in the interlayer also decreases with increasing t_{pulse} , from (for its front surface) 1,270 K to 500 K.

Despite the significant variation in peak electron temperatures in both the top layer and interlayer, the peak phonon temperature in both layers is minimally affected by t_{pulse} . As shown in Figs. 8b, e, and h, the peak phonon temperature at the front surface of the interlayer only slightly decreases from 505 K to 463 K when t_{pulse} increases from 0.04 ps to 10 ps, although the time required to reach the peak temperature notably increases from 1 ps to 10 ps, a direct consequence of the much slower heating in the latter case. Evidently, t_{pulse} has minimal impact on the existence of phonon heat backflow, and it does not significantly affect the peak phonon heat flux either, especially for $t_{pulse} < 1$ ps.

In conclusion, we emphasize that the significant impact of laser pulse duration on electron temperature arises from the laser's role as a direct heat source for electrons. Hence, it is logical to observe pronounced variations in electron temperature corresponding to the duration of the pulse, given that the heat source progressively energizes electrons over time.

In contrast, while the influence of laser pulse duration on phonon temperature is noticeable, it appears relatively weaker. This difference can be attributed to the distinct mechanism underlying phonon heating. Unlike electrons, which directly absorb energy from the laser, phonons primarily undergo heating through interactions with energized electrons, a process occurring within the timescale of the electron-phonon relaxation time.

In our investigation, the pulse durations examined (0.04, 0.39, 4, and 10 ps) are shorter or comparable to the electron-phonon relaxation time of Au, which typically ranges from 2 to 10 ps. Consequently, in the majority of scenarios explored in our study, electrons have nearly achieved equilibrium within themselves before significant phonon heating occurs. As a result, phonon temperature, directly influenced by electron temperature, displays less sensitivity to variations in laser pulse duration.

4. Conclusion

In this study, we employed the 2T-BTE approach to comprehensively model the lattice heat backflow phenomenon in bi-metallic-layer structures, focusing on Au-Pt and Au-Al layers supported on a silicon substrate. Notably, in this distinctive system, interlayers of Pt

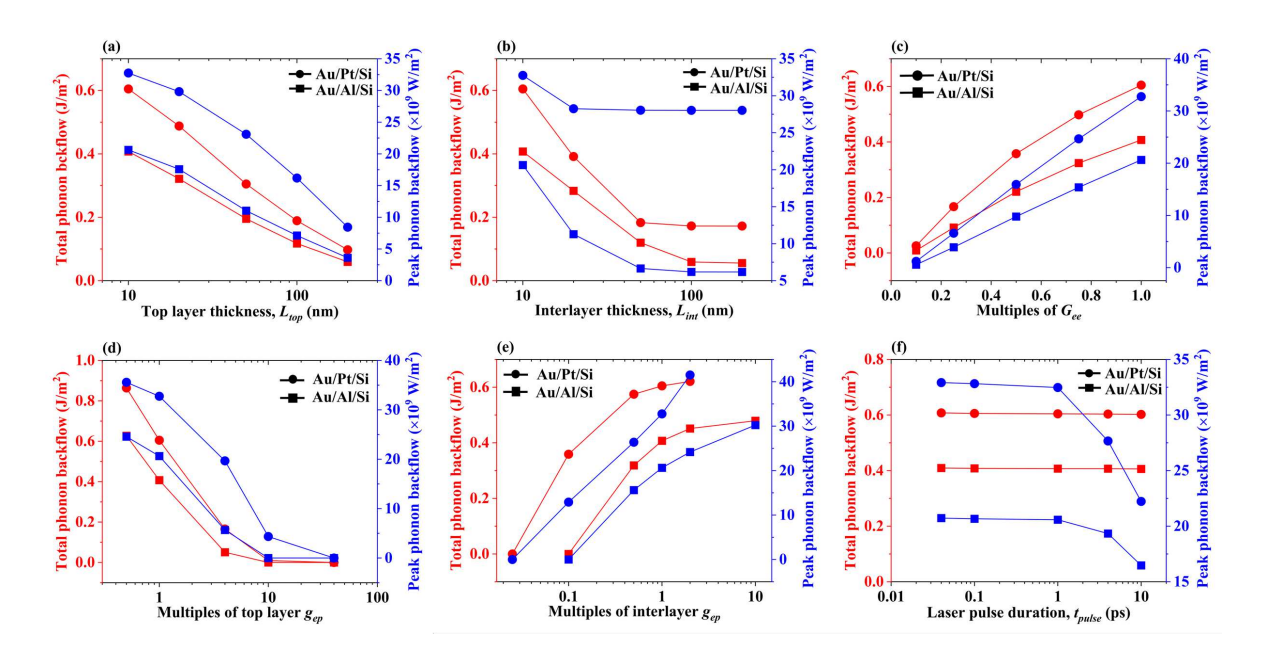


Figure 9: The effect of changes in structural and material parameters on total and peak phonon heat backflow for Au/Pt/Si and Au/Al/Si nanolayers.

or Al can attain a lattice temperature surpassing that of the directly exposed Au top layer, leading to a backflow of heat from the interlayer to the top layer. Our analysis delved into the impact of various structural and material parameters on the extent of heat backflow. As depicted in Fig. 9, a smaller top layer thickness L_{top} (panel a), smaller interlayer thickness L_{int} (panel b), increased electron thermal conductance G_{ee} between the top layer and interlayer (panel c), reduced electron-phonon coupling $g_{ep,top}$ in the top layer (panel d), and heightened electron-phonon coupling $g_{ep,int}$ in the interlayer (panel e) were identified to promote the lattice heat backflow phenomenon. Distinct from other parameters, the laser pulse duration t_{pulse} demonstrated a negligible impact on backflow for ultrashort pulses with $t_{pulse} < 1$ ps, as depicted in Fig. 9f. Nevertheless, we underscore that t_{pulse} directly influences the maximum electron temperature (Figs. 8a, d, and g), the scope of ultrafast-laser-induced Coulomb explosion, and other non-thermal phenomena not accounted for in our 2T-BTE simulations. Therefore, it remains essential to optimize t_{pulse} according to specific application requirements. As depicted by the simplified thermal circuit models in Fig. S7 of the Supplementary Materials, while $g_{ep,top} < g_{ep,int}$ establishes a necessary condition for the emergence of lattice heat backflow, other factors, including G_{ee} and layer thicknesses, exert significant influence

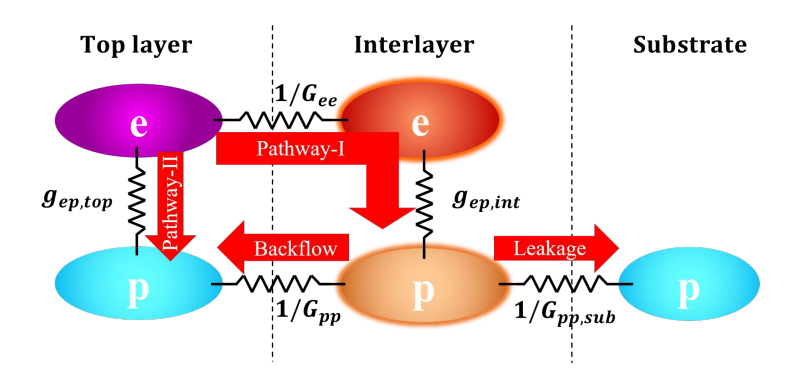


Figure 10: An approximate thermal circuit model of the bimetallic-layer-on-nonmetallic-substrate system studied in this work.

on the backflow dynamics.

In conclusion, for backflow to occur, the necessary condition $g_{ep,top} < g_{ep,int}$ must be satisfied so that more heat can be transferred to the interlayer (Pathway-I in Fig. 10) instead of to the top layer lattice (Pathway-II in Fig. 10). The thermal conductances at the top layer-interlayer interface, G_{ee} and G_{pp} , are the second important factors that determine the likelihood or magnitude of the lattice heat backflow. Specifically, the proper contact between the top layer and the interlayer can ensure efficient electron transport (i.e., high G_{ee}) from hot electrons in the top layer to those of the interlayer. While the phonon interfacial thermal conductance G_{pp} between the top layer and interlayer does not dictate the direction of heat flow at the interface, it does directly influence the magnitude of the phonon heat flux at the interface. Consequently, we conclude that to optimize lattice heat backflow, a bi-metallic-layer structure should be designed with a thin top layer featuring the weakest possible g_{ep} , at thin interlayer with the strongest possible g_{ep} , and efficient thermal contact between the two layers.

Lastly, it is worth noting that the silicon substrate utilized in our study had minimal impact on the overall thermal transport behavior within the bi-metallic layer structure. This is evidenced by the figures illustrating our BTE results (e.g., Figs. 6c, f, and i), which show only marginal changes in the temperature of the substrate. The limited influence of the substrate can be attributed to the lower phonon temperature typically observed at the rear surface of the interlayer (in contact with the substrate) compared to the front surface (in contact with the top layer), e.g., Figs. 6b, e, h. As a result, the leakage of lattice heat into the

substrate is substantially lower than the backflow to the top layer. However, it is plausible that the substrate could exert a significant effect on lattice heat backflow if it were composed of metal.

The insights gain from this study regarding lattice heat backflow behavior hold significant potential for enhancing the thermal design of optoelectronic devices and laser manufacturing processes that entail thermal interaction between multiple distinct metallic layers. These findings offer valuable guidance for experimentalists in selecting optimal structures and materials to showcase this intriguing electron-phonon coupled thermal transport phenomenon.

Acknowledgements

This work is supported by the National Science Foundation (NSF) EPSCoR Research Infrastructure Program (Award Number 2033424).

References

- [1] Y. Ju, M.-T. Hung, T. Usui, Nanoscale heat conduction across metal-dielectric interfaces (2006).
- [2] Z. Li, S. Tan, E. Bozorg-Grayeli, T. Kodama, M. Asheghi, G. Delgado, M. Panzer, A. Pokrovsky, D. Wack, K. E. Goodson, Phonon dominated heat conduction normal to mo/si multilayers with period below 10 nm, Nano letters 12 (6) (2012) 3121–3126.
- [3] A. Majumdar, P. Reddy, Role of electron–phonon coupling in thermal conductance of metal–nonmetal interfaces, Applied Physics Letters 84 (23) (2004) 4768–4770.
- [4] Y. Wang, X. Ruan, A. K. Roy, Two-temperature nonequilibrium molecular dynamics simulation of thermal transport across metal-nonmetal interfaces, Phys. Rev. B 85 (2012) 205311.
- [5] M. Mozafarifard, Y. Liao, Q. Nian, Y. Wang, Two-temperature time-fractional model for electron-phonon coupled interfacial thermal transport, International Journal of Heat and Mass Transfer 202 (2023) 123759.

- [6] T. Qiu, C. Tien, Femtosecond laser heating of multi-layer metals—i. analysis, International Journal of Heat and Mass Transfer 37 (17) (1994) 2789–2797.
- [7] L. Jiang, H.-L. Tsai, Improved two-temperature model and its application in ultrashort laser heating of metal films (2005).
- [8] Z. Lu, X. Ruan, Non-equilibrium thermal transport: a review of applications and simulation approaches, ES Energy & Environment 4 (2) (2019) 5–14.
- [9] B. Mueller, B. Rethfeld, Nonequilibrium electron–phonon coupling after ultrashort laser excitation of gold, Applied Surface Science 302 (2014) 24–28.
- [10] J. Chen, X. Xu, J. Zhou, B. Li, Interfacial thermal resistance: Past, present, and future, Rev. Mod. Phys. 94 (2022) 025002. doi:10.1103/RevModPhys.94.025002.
 URL https://link.aps.org/doi/10.1103/RevModPhys.94.025002
- [11] E. T. Swartz, R. O. Pohl, Thermal boundary resistance, Reviews of modern physics 61 (3) (1989) 605.
- [12] P. E. Hopkins, Multiple phonon processes contributing to inelastic scattering during thermal boundary conductance at solid interfaces, Journal of Applied Physics 106 (1) (2009).
- [13] K. Sääskilahti, J. Oksanen, J. Tulkki, S. Volz, Role of anharmonic phonon scattering in the spectrally decomposed thermal conductance at planar interfaces, Phys. Rev. B 90 (2014) 134312. doi:10.1103/PhysRevB.90.134312. URL https://link.aps.org/doi/10.1103/PhysRevB.90.134312
- [14] P. Chakraborty, I. A. Chiu, T. Ma, Y. Wang, Complex temperature dependence of coherent and incoherent lattice thermal transport in superlattices, Nanotechnology 32 (6) (2020) 065401. doi:10.1088/1361-6528/abc2ef.
 URL https://dx.doi.org/10.1088/1361-6528/abc2ef
- [15] Y. Wang, H. Huang, X. Ruan, Decomposition of coherent and incoherent phonon conduction in superlattices and random multilayers, Phys. Rev. B 90 (2014) 165406.

- doi:10.1103/PhysRevB.90.165406.
- URL https://link.aps.org/doi/10.1103/PhysRevB.90.165406
- [16] G. Xie, D. Ding, G. Zhang, Phonon coherence and its effect on thermal conductivity of nanostructures, Advances in Physics: X 3 (1) (2018) 1480417.
- [17] T. Ma, Y. Wang, Ex-situ modification of lattice thermal transport through coherent and incoherent heat baths, Materials Today Physics 29 (2022) 100884. doi:https://doi.org/10.1016/j.mtphys.2022.100884. URL https://www.sciencedirect.com/science/article/pii/S2542529322002826
- [18] P. E. Hopkins, L. M. Phinney, J. R. Serrano, T. E. Beechem, Effects of surface roughness and oxide layer on the thermal boundary conductance at aluminum/silicon interfaces, Phys. Rev. B 82 (2010) 085307. doi:10.1103/PhysRevB.82.085307. URL https://link.aps.org/doi/10.1103/PhysRevB.82.085307
- [19] T. S. English, J. C. Duda, J. L. Smoyer, D. A. Jordan, P. M. Norris, L. V. Zhigilei, Enhancing and tuning phonon transport at vibrationally mismatched solid-solid interfaces, Physical review B 85 (3) (2012) 035438.
- [20] S. Merabia, K. Termentzidis, Thermal boundary conductance across rough interfaces probed by molecular dynamics, Phys. Rev. B 89 (2014) 054309. doi:10.1103/PhysRevB.89.054309. URL https://link.aps.org/doi/10.1103/PhysRevB.89.054309
- [21] P. Chakraborty, L. Cao, Y. Wang, Ultralow lattice thermal conductivity of the random multilayer structure with lattice imperfections, Scientific reports 7 (1) (2017) 8134.
- [22] B. C. Gundrum, D. G. Cahill, R. S. Averback, Thermal conductance of metal-metal interfaces, Phys. Rev. B 72 (2005) 245426. doi:10.1103/PhysRevB.72.245426. URL https://link.aps.org/doi/10.1103/PhysRevB.72.245426
- [23] Y. Wang, X. Ruan, An evaluation of energy transfer pathways in thermal transport across solid/solid interfaces, in: Heat Transfer Summer Conference, Vol. 55478, American Society of Mechanical Engineers, 2013, p. V001T03A041.

- [24] B. F. Donovan, C. J. Szwejkowski, J. C. Duda, R. Cheaito, J. T. Gaskins, C.-Y. Peter Yang, C. Constantin, R. E. Jones, P. E. Hopkins, Thermal boundary conductance across metal-gallium nitride interfaces from 80 to 450 k, Applied Physics Letters 105 (20) (2014).
- [25] Y. Wang, Z. Lu, A. K. Roy, X. Ruan, Effect of interlayer on interfacial thermal transport and hot electron cooling in metal-dielectric systems: An electron-phonon coupling perspective, Journal of Applied Physics 119 (6) (2016).
- [26] E. Black, J. Bain, T. Schlesinger, Thermal management in heat-assisted magnetic recording, IEEE transactions on magnetics 43 (1) (2006) 62–66.
- [27] Z. Lu, Y. Wang, X. Ruan, Metal/dielectric thermal interfacial transport considering cross-interface electron-phonon coupling: Theory, two-temperature molecular dynamics, and thermal circuit, Physical Review B 93 (6) (2016) 064302.
- [28] A. Giri, J. T. Gaskins, B. F. Donovan, C. Szwejkowski, R. J. Warzoha, M. A. Rodriguez, J. Ihlefeld, P. E. Hopkins, Mechanisms of nonequilibrium electron-phonon coupling and thermal conductance at interfaces, Journal of Applied Physics 117 (10) (2015).
- [29] X. Li, W. Park, Y. Wang, Y. P. Chen, X. Ruan, Reducing interfacial thermal resistance between metal and dielectric materials by a metal interlayer, Journal of Applied Physics 125 (4) (2019).
- [30] S. M. Oommen, L. Fallarino, J. Heinze, O. Hellwig, S. Pisana, Role of vibrational properties and electron—phonon coupling on thermal transport across metal-dielectric interfaces with ultrathin metallic interlayers, Journal of Physics: Condensed Matter 34 (46) (2022) 465701.
- [31] G. Lin, L. Jiang, P. Ji, The effect of enhanced heat transfer across metal–nonmetal interfaces subject to femtosecond laser irradiation, Physical Chemistry Chemical Physics 25 (29) (2023) 19853–19867.
- [32] G.-M. Choi, R. Wilson, D. G. Cahill, Indirect heating of pt by short-pulse laser irradiation of au in a nanoscale pt/au bilayer, Physical Review B 89 (6) (2014) 064307.

- [33] L. Guo, S. L. Hodson, T. S. Fisher, X. Xu, Heat transfer across metal-dielectric interfaces during ultrafast-laser heating (2012).
- [34] Z. Lin, L. V. Zhigilei, V. Celli, Electron-phonon coupling and electron heat capacity of metals under conditions of strong electron-phonon nonequilibrium, Physical Review B 77 (7) (2008) 075133.
- [35] S. S. Ghai, W. T. Kim, R. A. Escobar, C. H. Amon, M. S. Jhon, A novel heat transfer model and its application to information storage systems, Journal of Applied Physics 97 (10) (2005).
- [36] F. N. Donmezer, D. Singh, W. James, A. Christensen, S. Graham, J. Y. Murthy, Lattice boltzmann and discrete ordinates methods for phonon transport modeling: A comparative study 54969 (2011) 333–343.
- [37] P. E. Hopkins, P. M. Norris, Substrate influence in electron–phonon coupling measurements in thin au films, Applied Surface Science 253 (15) (2007) 6289–6294.